# VICIRS
# Development of vicarious calibration tools for MWI and ICI using radiosoundings (VICIRS)

**D15:** Algorithm Theoretical Basis Document

| | |
|---|---|
| **Deliverable #** | D15 |
| **Doc type** | Technical report |
| **Responsible** | Elisabetta Ricciardelli |
| **Authors** | Domenico Cimini<br>Francesco Di Paola<br>Sabrina Gentile<br>Salvatore Larosa<br>Fabio Madonna<br>Mario Montopoli<br>Elisabetta Ricciardelli<br>Filomena Romano<br>Mariassunta Viggiano |

**Date**: 15 April 2024

## TABLE OF CONTENTS

# 1. Introduction

As required in the generic Statement of Work (SoW) ([AD-1], R-39/R-40), the methodology and the criteria used for the selection and comparison of data are described in this Algorithm Theoretical Basis Document (ATBD). The ATBD contains the satellite instrument description, the radiosonde archive description, the analysis of data to be used for cal/val process, the matchup analysis, the bias and uncertainty analysis and the multi-source correlative methodology analysis.

## 1.1 Applicable documents

[AD-1] Statement of Work, Study on the development of vicarious calibration tools for MWI and ICI using radiosoundings. EUM/RSP/SOW/22/1290081, Issue v1B, 22 June 2022.
[AD-2] ICI Calibration and Validation Plan, EUM/LEO-EPSSG/PLN/17/776069 v1D.
[AD-3] MWI Calibration and Validation Plan, EUM/LEO-EPSSG/PLN/14/776068 v1F.
[AD-4] MWI L1B Product Format Specification, EUM/LEO-EPSSG/SPE/14/767115 v4
[AD-5] ICI L1B Product Format Specification, EUM/LEO-EPSSG/SPE/14/771723 v4
[AD-6] EPS-SG Programme Overall Calibration and Validation Plan, EUM/LEO-EPSSG/PLN/14/758341
[AD-7] D05 Critical review of the literature methods
[AD-8] D07 Report on methodologies analysis
[AD-9] D09 Report on the development of VICIRS tool
[AD-10] D10 Report on VICIRS-tool software description and user/installation guide

## 1.2 Acronyms

Abbreviations specific to this document are listed in the following table.

| Acronyms | Definition |
|---|---|
| AMD | Air Motion Displacement |
| BT | Brightness Temperature |
| $BT_O$ | Observed BT (by satellite-based sensor) |
| BTs | Simulated BT |
| BT_TA | average of the FOVs-BT included in TA |
| DL | Dedicated Launch |
| FOV | Field Of View |
| GRUAN | Global Climate Observing System Reference Upper-Air Network |
| ICI | Ice Cloud Imager |
| LF | Land Fraction |
| LSE | Land Surface Emissivity |
| MCM | Multi-source Correlative Methodology |
| MWI | Microwave Imager |
| NWP | Numerical Weather Prediction |
| numTA | Number of TA types |
| P | Pressure |
| Pmin | minimum pressure level |
| RH | Relative Humidity |
| RHARM | Radiosounding HARMonization |

| | |
|---|---|
| RS | Radiosounding |
| RTTOV | Radiative Transfer for TOVS |
| SD | Standard Deviation |
| T | Temperature |
| TA | Target Area |
| TC | Triple Collocation |
| Tskin | Skin Temperature |
| T2m | Temperature at 2 meter |
| uBT | BT uncertainty |
| SD_TA | SD corresponding to BT_TA |
| surftypeM | RS surface-type (0=sea, 1=land, 2=mixed) determined on the basis of MWI-FOVs LF |
| surftypeI | RS surface-type (0=sea, 1=land, 2=mixed) determined on the basis of ICI-FOVs LF |
| SAT | Generic for MWI and ICI |
| VICIRS | VIcarious Calibration for MWI and ICI using RadioSoundings |

# 2. Data description

## 2.1 MWI and ICI description

The VIcarious Calibration for MWI and ICI using RadioSoundings (VICIRS) tool has been developed to validate the observations of the two conical-scanning radiometers committed to fly from 2025 onwards aboard the METOP-SG (Second Generation) satellites as part of the EUMETSAT Polar System (EPS) program. These radiometers are the Microwave Imager (MWI) and the Ice Cloud Imager (ICI). ICI will observe at 13 channels in 11 frequency bands. ICI will be the first operational sensor covering the mm/sub-mm wavelengths from 183 to 664 GHz, bridging a “spectral gap” between the microwaves and the far infrared. Its main objective will be (i) the provision of ice cloud products for climate monitoring, (ii) support the validation of the representation of ice clouds in weather/climate models, (iii) information on non-precipitating ice. ICI footprint resolution is 16 km for all the frequencies. The footprint overlap is ≥20% and the spatial sampling is about 9 km along track and 2.5 km across track. MWI will observe at 26 channels in 18 frequency bands between 18 and 183 GHz. All channels up to 89 GHz will observe in dual polarization, while only vertical polarization will be provided for higher frequencies. The combined use of MWI and ICI radiometers will provide an unprecedented set of microwave passive measurements, from 18.7 GHz up to 664 GHz. MWI main applications are (i) provision of cloud/precipitation products in support of regional/global NWP, (ii) continuity of measurements of key microwave imager channels in support of long-term climate records, (iii) observations of ocean surface parameters (wind speed, sea ice). MWI footprint resolution is 50 km for 18.7 and 23.8 GHz, 30 km for frequencies from 31.4 GHz to 53.75 GHz and 10 km for frequencies from 118.75 GHz to

183.31 GHz. The footprint overlap is ≥20% and the spatial sampling is about 9 km along track and 2.5 km across track.

## 2.2 Radiosonde archive description

VICIRS tool compares MWI/ICI Brightness Temperature (BT) with BTs simulated from radiosonde profile by the GRUAN processor (Carminati et al., 2019) adapted to the purposes of VICIRS (v6.3.b.1.0.0). Radiosoundings (RS) are collected from two archives, GRUAN and RHARM, which are described in the following sub-sections.

### 2.2.1 GRUAN archive description

Homogenous upper-air data records with quantified uncertainties are the ideal candidate for the MWI/ICI calibration plan. As such, the primary dataset for the MWI and ICI calibration is the Global Climate Observing System (GCOS) Reference Upper-Air Network (GRUAN), which provides homogeneous and fully traceable upper-air measurements with quantified uncertainties. GRUAN was established in 2006 (Bodeker et al, 2015) and it provides long-term, high-quality radiosounding data at several sites worldwide. Although the GRUAN network includes 31 sites, data from 18 sites are routinely archived, of which 14 sites are certified to date. GRUAN measurements include uncertainties and are traceable to the SI international or other accepted standards, providing extensive metadata and comprehensive documentation of measurements and algorithms (Dirksen et al., 2014, Von Rhoden et al., 2021). Moreover, GRUAN includes the balloon position at all pressure/height levels using GNSS positioning. GRUAN is currently providing three radiosonde data products for four different types of radiosondes (Vaisala RS92 and RS41, Meisei iMS-100 and RS11-G). Although GRUAN represents the highest quality radiosounding product available at global scale, its spatial coverage may be insufficient for the purpose of ensuring calibration in various climate regimes and horography conditions. Therefore, an additional dataset recently provided within the Copernicus Climate Change Service (C3S), named Radiosounding HARMonization (RHARM, Madonna et al., 2022), was considered.

### 2.2.2 RHARM archive description

Building on the GRUAN expertise and WMO radiosonde intercomparison data, RHARM provides adjusted radiosounding observations of temperature, humidity and wind with estimated uncertainties at 700 stations, plus launches from a number of ships. The RHARM algorithm mimics the GRUAN procedure to process RS92 sonde types (other types are under implementation). RHARM also uses the 2010 WMO/CIMO radiosonde intercomparison data set to adjust the bias and estimate measurement uncertainties for several radiosonde types not covered at present by the GDPs.

The RHARM dataset includes twice daily (0000 and 1200 UTC) bias-adjusted radiosonde data at pressure levels in the range 1,000–10 hPa, from 1978 to present, using as input data source the Integrated Global Radiosonde Archive (IGRA), provided and maintained by the NOAA-NCEI. The applied adjustments are interpolated to all reported levels, when these are provided in IGRA and in the high-resolution BUFR files made available at a larger number stations since 2014, the latter used an additional data and metadata source provided directly from ECMWF. RHARM is the first data set to provide homogenized time series with an estimation of the observational uncertainty at each sounding pressure level. By construction, RHARM adjusted fields are not affected by cross-contamination of biases across stations and are fully independent of reanalysis data. In the upcoming new version of RHARM, also the exact balloon position at all pressure/height levels will be derived from its latitude and longitude estimations, obtained from the GNSS signal, or from the wind data.

Currently using IGRA version 2 dataset as input, the RHARM data set inherits the IGRA quality assurance procedures (Durré et al., 2008). Nevertheless, RHARM applies additional quality checks on: the metadata availability; physical plausibility; data completeness check; accuracy of the bias adjustment; removal of outliers; vertical correlation between structural breaks at the same station; coherency check for the adjustments applied at the significant levels.

The RHARM dataset is currently available via the Copernicus Climate Data Store (CDS) (https://cds.climate.copernicus.eu/cdsapp#!/dataset/insitu-observations-igra-baseline-network?tab=overview). The dataset is updated annually. In the near future, there is a plan to increase the monthly updates, depending only on the constraints applied by the CDS team, as the software generating the RHARM data can be operated in an operational fashion. This means that data can possibly be provided in NRT with a typical 1day delay, the data update frequency for IGRA.

## 2.3 Numerical Weather Prediction retrieve

The NWP data can be used in the GRUAN processor to simulate the BT and the associated uncertainty from RS profiles as a complement for missing fields in the RS datasets (such as surface parameters or data over the RS top level). NWP is mandatory in the framework of the multi-source correlative analysis.

The NWP used for the study is the ECMWF Integrated Forecasting System at highest spatial resolution (called HRES, with horizontal grid spacing of about 0.125°). ECMWF files are downloaded from the Meteorological Archival and Retrieval System (MARS) through the ECS system, which is accessible exclusively to registered users from Member and Co-operating States.

The characteristics of NWP files are set in a batch script: *date* and *time* select the simulation temporally closest before the RS launch time available in the archive, *step* indicates the hours of forecasts, the first 15 hours of forecast are downloaded with a step of 3 hours. A 2°x2° square (about 16*16 grid points) around the launch site is chosen as *area* and the profile variables are downloaded on the 137 model levels (*levt*). The single level atmospheric fields selected are sea ice area fraction (131), geopotential (129), surface pressure (134), 10-meter U wind component (165), 10-meter V wind component (166), 2-meter temperature (167), 2-meter dew point temperature (168), land-sea mask (172), and skin temperature (235), and total cloud cover (164). The model level atmospheric profiles downloaded are temperature (130), U component of wind (131), V component of wind (132), specific humidity (133), logarithm of surface pressure (152), fraction of cloud cover (248), and ozone mass mixing ratio (203).
MARS archive contains the forecast runs out to 10 days based on the 00/12 UTC analysis forecast, while the 06 and 18 forecast runs are not archived.
The size of the single NWP file containing all the 15 hours of forecast is about 6-8 Mb and it is usually downloaded in 5-10 min depending on the crowding condition of the MARS system. The procedure to download the NWP files is completely automatic in the VICIRS tool.

# 3. Radiosounding analysis and quality check

The RS analysis is mandatory to check whether the related match-up is usable for calibration purposes. The quality check of RS is done in terms of numbers of levels (n) and minimum pressure (Pmin) value, air mass displacement (AMD), cloud contamination. In detail, RS is considered for the calibration process when:

- n$\geq 40$ for P/T/RH profiles and the uncertainties are available for each profile and for all the n pressure levels;
- is Pmin≤10hPa ([AD-8], Section 5);
- RS is in clear sky. The presence of cloudy layers is verified by comparing the RH values with the reference values for clear sky as determined by Zhang et al. (2010). Note that this method was developed for RS92 sonde, but its performances with RS41 have been assessed (see [AD-8], Section 3.2). It outputs the number of levels contaminated by low, middle and high clouds;
- AMD $\leq TA\, radius$. ([AD-8], Section 3.2) AMD is determined by multiplying the temporal distance between the satellite overpass and sonde launch, $\Delta t$, by the wind speed average between 700 hPa and 300 hPa, $\underline{w}$ (following Buehler et al. 2004, Brobyshev et al. 2017, Moradi et al. 2010). AMD test is used to reduce the variability caused by the horizontal inhomogeneity of the atmosphere.

When the NWP option is activated in *config.ini*, the NWP profile is checked for cloud contamination. In detail, the NWP profile spatially and temporally closest to the radiosonde launch is checked for the presence of low medium or high cloud layer by examining the NWP field *lcc* (fraction of low cloud cover in the NWP profile), *mcc* (fraction of medium cloud cover in the NWP profile) and *hcc* (fraction of high cloud cover in the NWP profile). When the NWP profile is cloudy (hcc+lcc+mcc>0), it is not considered in the calibration process that will continue considering only RS, unless the user decides to discard the related match-up from the calibration process.

# 4. Target Area analysis

The spatial collocation criteria adopted in VICIRS tool is based on the target area (TA) approach ([AD-7], Section 2.2.1). This approach is preferred to the single closest (SC) one because it takes in account the radiosonde drift and it allows to minimize the representativeness error due to the spatial and temporal collocation by applying homogeneity test and AMD test ( [AD-7] Section 2.2.1 and Section 5.2.3).

## 4.1 Data spatial and temporal collocation

Generally, TA is a circle with a radius of 50 km centered at the radiosonde launch site (Buehler et al. 2004, Moradi et al. 2010, Bobryshev et al. 2018) with the related BT (hereinafter referred to $BT_{TA}$ ) defined as the average of the FOV-BTs included in it.

$$BT_{TA} = \sum_{i=1}^{N} BT_i \cdot \lambda_{i,j}$$

where N is the number of the MWI/ICI FOVs included in the TA and $\lambda_{i,j}$ is the weight for the $i^{th}$ FOV:

$$\lambda_{i,j} = \frac{d_{0i}^{-j}}{\sum_{i=1}^{N} d_{0i}^{-j}}$$

5 types of TA are obtained by modifying TA definition and by varying j $\lambda_{i,j}$ (the larger *j* is, the larger the weight of the FOVs closest to the launch site):

- **TA type 1: circular TA** where $BT_{TA}$ is determined as the average of the BT of the FOVs included in TA (**j=0**);
- **TA type 2: circular TA** where $BT_{TA}$ is determined for **j=1** (inverse distance weight);
- **TA type 3: circular TA** where $BT_{TA}$ is determined for **j=2** (inverse squared distance weight);

- **TA type 4: drift-based exact TA** as the set of FOVs closest to each pressure level of the radiosonde path (nearest neighbour approach), $BT_{TA}$ is determined for **j=1;**
- **TA type 5: 3x3 exact TA** as the set of the 9 FOVs closest to each RS pressure level, consisting of the FOV closest to the RS pressure level + the 8 FOVs closest to it.

The *TA-radius* is set equal to the maximum *sonde-drift* if sonde-drift<=50 km, otherwise *TA-radius*=50 km.

The **drift-based TA** (types 4 and 5) can be used only when the latitude and longitude are available for each pressure level (GRUAN RS). The number of FOVs included in the drift-based TA is lower than that in the circular TA. In this way, a match-up considered cloudy on the basis of circular TA may be identified as not-cloudy on the basis of drift-based TA if it does not include the cloudy FOVs present in the circular TA. As a result, the number of match-ups may be higher when drift-based TA is chosen.

The temporal collocation will consider three options for the temporal distance between the sonde launch time and the satellite overpass ($\Delta T$):

1. -15'≤ $\Delta T$ ≤45'
2. -1 hour ≤ $\Delta T$ ≤1 hour
3. -3 hours ≤ $\Delta T$ ≤3 hours.

The 3 temporal options are all configurable in the VICIRS tool (*config.ini* for collecting match-ups and *query.ini* for match-up and bias/uncertainty analysis).

## 4.2 Cloud screening methodology for MWI and ICI

The MW cloud mask threshold tests available in literature ([AD-7] sub-section 2.2.3) are being adapted and applied to the simulated MWI and ICI level 1B. The threshold tests used for MWI and ICI are listed in Table 4.1 and 4.2 respectively.
In detail, ICI and MWI Test 1 is based on the threshold test proposed for 183.31.31$\pm$1 GHz and 183.31.31$\pm$7 GHz AMSU-B band from Buehler at al. (2007). The frequency at 183.31.31$\pm$1 GHz is replaced with 183.31.31$\pm$2 GHz for ICI and MWI. The threshold value for $BT_{183.31\pm 2GHz}$ has been chosen similar to that proposed by Buehler et al. (2007), valid for AMSU viewing angle of 44.5° measurements, this choice has been done by taking into account the ICI/MWI constant incidence angle of 53.1°. As ICI and MWI are conically scanning instruments with constant incidence angle, there is no need to adapt the thresholds for off nadir measurements.
MWI-Test 1 and MWI-Test 2 related to 89 GHz and 165 GHz frequencies, respectively, are based on threshold tests proposed by Yaping et al. (2018). Yaping et al. (2018) tested the proposed-criteria to detect deep convective clouds on BT at 89 GHz (v-polarization)

and 165 GHz (instead of AMSU-B 150 GHz frequency) and selected the 89 and 150 GHz threshold values from a BT 3-year-dataset of AMSU-B observations acquired in summer.

**Table 4.1** Cloud tests for MWI

| MWI | 183 GHz frequencies | 89 Ghz frequency | 165 Ghz frequency |
|---|---|---|---|
| **Test 1(a)** | $(a) BT_{183.31\pm 2GHz} < 235.2\ K\ and\ (BT_{183.31\pm 7.0GHz}$-$BT_{183.31\pm 2GHz})0$ **(Buehler et al., 2007)** | $BT_{89GHz,v} < 240\ K$ **(by Yaping et al. (2008), over land)** | $BT_{165GHz} < 220\ K$ **by Yaping et al. (2008);** |
| **Test 1(b)** | $(b)\ BT_{183.31\pm 2GHz} < 235.2\ K\ and\ (BT_{183.31\pm 3.4GHz}$-$BT_{183.31\pm 2GHz}) < 0$ ***(Buehler et al. 2007)*** | | |
| **Test 2** | $(BT_{183.31\pm 2.0GHz}$-$BT_{183.31\pm 7GHz}) \geq 0\ and\ (BT_{183.31\pm 2.0GHz} - BT_{183.31\pm 3.4GHz}) \geq 0\ and\ (BT_{183.31\pm 3.4GHz} - BT_{183.31\pm 7GHz}) \geq 0$ ***(Hong et al. 2005, to detect deep convective clouds);*** | $1 < BT_{89GHz,v} - BT_{89GHz,h} < 5\ K$ $and\ BT_{89GHz,v} < 265\ K$ *(over land);* $BT_{89GHz,v} - BT_{89GHz,h} \leq 20$ *(over sea)* ***(based on Gong and Wu, 2017)*** | |
| **Test 3** | $(BT_{183.31\pm 2.0GHz}$-$BT_{183.31\pm 7GHz}) \geq (BT_{183.31\pm 2.0GHz} - BT_{183.31\pm 3.4GHz}) \geq (BT_{183.31\pm 3.4GHz} - BT_{183.31\pm 7GHz}) > 0$ **(Hong et al. 2005, to detect convective overshooting);** | | |
| **Test 4** | $BT_{183.31\pm 2.0GHz} > BT_{183.31\pm 3.4GHz} > BT_{183.31\pm 4.9GHz} > BT_{183.31\pm 6.1GHz} > BT_{183.31\pm 7GHz}$ *(***based on Clain et al. 2005);*** | | |

MWI Test 2 on 89 GHz frequency (v, h polarization) and ICI Test 1 on 664 GHz (v and h polarization), are based on the study of Gong and Wu (2017). By examining the ice cloud scenes identified by the test on 183.31 GHz band (identified by the "3$\sigma$ method" proposed by Gong and Wu (2017) and described in AD-7 sub-section 2.2.3), they found that the scattering by frozen particles was highly polarized, with v–h polarimetric differences (PD) being positive. In particular, the PD amplitude for 166 and 89 GHz peaks at about 10 K in the tropics and it increases slightly with latitude, both over sea and land (Figure 4 in Gong and Wu, (2017)). They observed small values for the difference between vertical and horizontal polarized frequency along deep convective lines and higher values in the anvil and precipitation region, with more evidence at 166 than 89 GHz frequency, because of the increasing contribution of ice-particle scattering at the higher MW frequencies. In this work some simplifications regarding the orientation of ice hydrometeors are used. The higher values in the anvil and stratiform precipitation areas are due to the absence of multiple scattering processes that saturates the polarization signatures. Since the scattering between ice hydrometeors and radiation induces a remarkable polarization signature strongly dependent on the size, shape, and orientation of non-spherical ice hydrometeors, a more comprehensive discussion of this topic is needed and can be found in Barkalas et al. (2021). Moreover, at 89 GHz the difference between v and h polarization is more sensitive to signals from the underlying surface, especially from sea. To investigate the cirrus clouds (ice clouds with small ice-crystals), they considered the higher frequency at 640 GHz, acquired by the NASA airborne Compact Scanning Submillimeter-wave Imaging Radiometer (CoSSIR) (Evans et al., 2005). Approximately, they found a value of 10 K for the peak of difference between BT at v and h polarization occurring at 220 K for 89 GHz and at 200 K for 640 GHz.

**Table 4.2** Cloud tests for ICI

| ICI | 183 GHz frequencies | 664v GHz frequency |
|---|---|---|
| **Test 1(a)** | $BT_{183.31\pm 2GHz} < 240\ K\ and\ (BT_{183.31\pm 7.0GHz}$-$BT_{183.31\pm 1GHz}) < 0$ ***(Buehler et al., 2007)*** | $BT_{664v\ GHz} < 220\ K$ ***(based on Gong and Wu, 2017)*** |
| **Test 1(b)** | $BT_{183.31\pm 2GHz} < 240\ K\ and\ (BT_{183.31\pm 3.4GHz}$-$BT_{183.31\pm 1GHz}) < 0$ ***(Buehler et al., 2007)*** | |
| **Test 2** | $(BT_{183.31\pm 2.0GHz}$-$BT_{183.31\pm 7GHz}) \geq 0\ and\ (BT_{183.31\pm 2.0GHz} - BT_{183.31\pm 3.4GHz}) \geq 0\ and\ (BT_{183.31\pm 3.4GHz} - BT_{183.31\pm 7GHz}) \geq 0$ ***(Hong et al., 2005, to detect deep convective clouds)*** | $BT_{664v\ GHz} < 225\ K\ and\ 0 \leq\ BT_{664v\ GHz} - BT_{664h\ GHz} < 15K$ ***(based on Gong and Wu, 2017)*** |
| **Test 3** | $(BT_{183.31\pm 2.0GHz}$-$BT_{183.31\pm 7GHz}) \geq\ (BT_{183.31\pm 2.0GHz} - BT_{183.31\pm 3.4GHz}) \geq\ (BT_{183.31\pm 3.4GHz} - BT_{183.31\pm 7GHz}) > 0$ ***(Hong et al., 2005, to detect convective overshooting)*** | |
| **Test 4** | $BT_{183.31\pm 2.0GHz} > BT_{183.31\pm 3.4GHz} > BT_{183.31\pm 7GHz}$ ***(based on Clain et al., 2015)*** | |

## 4.3 Emissivity screening considerations

Among the geophysical inputs required by the radiative transfer model (RTM) to simulate MW-BTs from the radiosonde profiles, the land surface emissivity (LSE) needs a particular attention because of the complexity to model it. Several approaches to emissivity analysis for MW observations are described in sub-section 2.2.2 of [A-7].
Surface emissivity models, such as the TELSEM2 (Wang et al., 2017) and TESSEM2 (Prigent et al., 2017), are distributed with the current version of RTTOV. In detail,

TESSEM2 provides parameterized sea surface emissivity, TELSEM2 provides parameterized land, snow and sea-ice surface emissivity. Both models have been extended with respect to their previous versions to cover the range up to 700 GHz and they are suitable for MWI and ICI simulations (Sub-section 5.2.4 of [A-7]). Since RTTOV v13.2 (released in December 2022) a new option is available, namely the SURface Fast Emissivity Model for Ocean (SURFEM-Ocean). SURFEM-Ocean (Kilic et al., 2023) is a fast neural network parameterization of the PARMIO physical reference emissivity model simulating all Stokes components for channels in the range 0.5 – 700 GHz (Dinnat et al., 2023). To avoid uncertainties due to incorrect parameterization of LSE for the frequencies affected by LSE, the emissivity analysis will be applied to the clear sky match-ups considered in the calibration process.

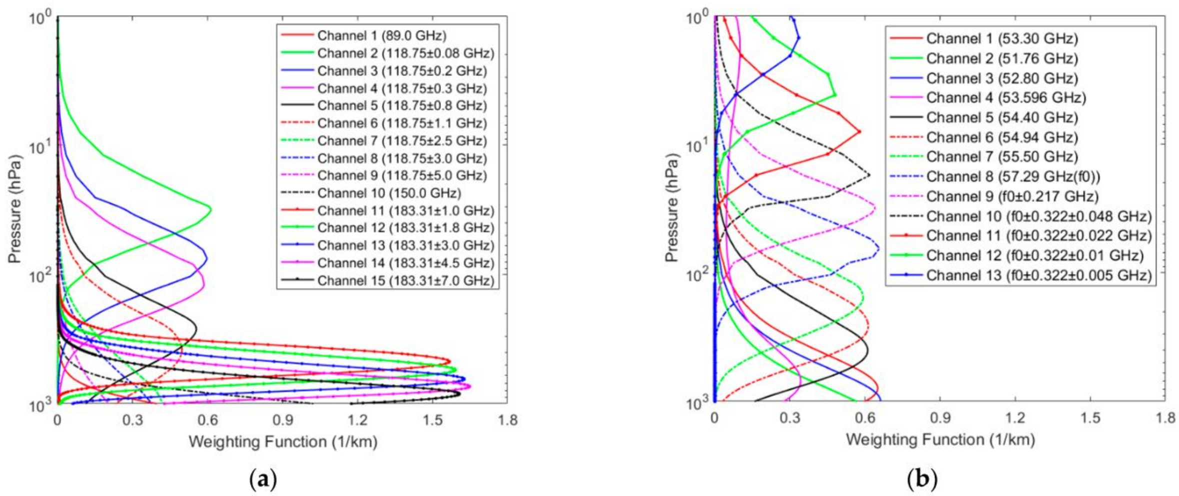


**Figure 4.1**. Weighting functions for 89-183 GHz channels (a) and 51-58 GHz channels (b) (He et al. 2022).

The required performances for MWI and ICI are listed in Tables 4.3.1 and 4.3.2. In general, the observations at ICI frequencies (Table 4.3.2) are not affected by LSE because of the high atmospheric opacity. However, in very dry conditions (e.g. subarctic-winter conditions), few channels are sensitive to the surface contribution. This is the case of (i) the three outermost 183 GHz channels, (ii) the channel at 243 GHz, and (iii) the outermost 325 GHz channel (Buehler et al. 2012).

**Table 4.3.1** Required MWI performances (from AD-3)

| *Channel* | *Frequency (GHz)* | *Bandwidth(MHz)* | *NEDT (K)* | *Radiometric Bias (K)* | *Polarization* | *Footprint Size at 3dB (km)* |
|---|---|---|---|---|---|---|
| MWI-1 | 18.7 | 200 | 0.8 | 1.0 | V, H | 50 |
| MWI-2 | 23.8 | 400 | 0.7 | 1.0 | V, H | 50 |
| MWI-3 | 31.4 | 200 | 0.9 | 1.0 | V, H | 30 |

| | | | | | | |
|---|---|---|---|---|---|---|
| MWI-4 | 50.3 | 180 | 1.1 | 1.0 | V, H | 30 |
| MWI-5 | 52.7 | 180 | 1.1 | 1.0 | V, H | 30 |
| MWI-6 | 53.24 | 400 | 1.1 | 1.0 | V, H | 30 |
| MWI-7 | 53.750 | 400 | 1.1 | 1.0 | V, H | 30 |
| MWI-8 | 89.0 | 4000 | 1.1 | 1.0 | V, H | 10 |
| MWI-9 | 118.7503±3.20 | 2x500 | 1.3 | 1.0 | V | 10 |
| MWI-10 | 118.7503±2.10 | 2x400 | 1.3 | 1.0 | V | 10 |
| MWI-11 | 118.7503±1.40 | 2x400 | 1.3 | 1.0 | V | 10 |
| MWI-12 | 118.7503±1.20 | 2x400 | 1.3 | 1.0 | V | 10 |
| MWI-13 | 165.5±0.75 | 2x1350 | 1.2 | 1.0 | V | 10 |
| MWI-14 | 183.31±7.0 | 2x2000 | 1.3 | 1.0 | V | 10 |
| MWI-15 | 183.31±6.1 | 2x1500 | 1.2 | 1.0 | V | 10 |
| MWI-16 | 183.31±4.9 | 2x1500 | 1.2 | 1.0 | V | 10 |
| MWI-17 | 183.31±3.4 | 2x1500 | 1.2 | 1.0 | V | 10 |
| MWI-18 | 183.31±2.0 | 2x1500 | 1.3 | 1.0 | V | 10 |

The RS from GRUAN sites on island (i.e., Tenerife (TEN), Graciosa (GRA) and Minatorishima (MIT)) will be used to calibrate the MWI channels affected by LSE. Most likely, these correspond to the first four channels (18.7, 23.8, 31.4, and 50.5 GHz), as well as 52.61, 53.24, 53.75, 89 GHz and 165.5 GHz in high latitude, that could be differently affected by LSE as it figures out from the weighting function in Figure 4.1. Similarly, particular attention must be paid also to MWI less opaque frequencies in the 118.75 GHz absorption band (e.g. 118.75±3.2 GHz).

**Table 4.3.2** ICI channels characteristics

| ***Channel*** | ***Frequency (GHz)*** | ***Bandwidth (MHz)*** | ***NEDT (K)*** | ***Radiometric Bias (K)*** | ***Polarization*** | ***Footprint Size at 3dB (km)*** |
|---|---|---|---|---|---|---|
| ICI-1 | 183.31±7.0 | 2x2000 | 0.8 | 1 | V | 16 |
| ICI-2 | 183.31±3.4 | 2x1500 | 0.8 | 1 | V | 16 |
| ICI-3 | 183.31±2.0 | 2x1500 | 0.8 | 1 | V | 16 |
| ICI-4 | 243.2±2.5 | 2x3000 | 0.7 | 1.5 | V, H | 16 |
| ICI-5 | 325.15±9.5 | 2x3000 | 1.2 | 1.5 | V | 16 |

| | | | | | | |
|---|---|---|---|---|---|---|
| ICI-6 | 325.15±3.5 | 2x2400 | 1.3 | 1.5 | V | 16 |
| ICI-7 | 325.15±1.5 | 2x1600 | 1.5 | 1.5 | V | 16 |
| ICI-8 | 448±7.2 | 2x3000 | 1.4 | 1.5 | V | 16 |
| ICI-9 | 448±3.0 | 2x2000 | 1.6 | 1.5 | V | 16 |
| ICI-10 | 448±1.4 | 2x1200 | 2.0 | 1.5 | V | 16 |
| ICI-11 | 664±4.2 | 2x5000 | 1.6 | 1.5 | V, H | 16 |

A useful test for screening MWI/ICI observations affected by LSE is the homogeneous test, consisting in comparing the SD_TA with the radiometric noise NE$\Delta T$ and classifying as inhomogeneous the TAs with SD_TA > NE$\Delta T$ (Buehler et al. 2004). The homogeneous-flag is an information provided by the TA analysis that does not cause the inhomogeneous TA to be removed. The NE$\Delta T$ associated to the sample ($NE\Delta T_{sample}$) must be used, while $NE\Delta T$ in Table 4.3.1 for MWI and Table 4.3.2 for ICI is associated to the footprint ($NE\Delta T_{footprint}$). In fact, along-scan several samples within the footprint of each channel are taken (oversampling). As such, convolution of samples reduces the associated radiometric noise. $NE\Delta T_{sample}$ is simply derived from $NE\Delta T_{footprint}$ by considering the oversampling factor $1/K_{NE\Delta T}$, which is channel dependent (j indicates the channel index):

$$NE\Delta T_{sample} = NE\Delta T_{footprint}/K_{NE\Delta T}(j)$$

where:

$K_{NE\Delta T}(j) = \sqrt{\frac{T_{int}}{T_{int3dB}(j)}}$, $T_{int}$ is the sample integration time and $T_{int3dB}$ is the channel-dependent integration time over the 3dB antenna footprint.

These numbers have been provided by EUMETSAT for MWI:

$T_{int}$ = 0.394 ms

$T_{int3dB}$ = [8.47 8.47 8.189 8.189 5.225 5.225 4.165 4.165 4.165 4.165 4.165 4.165 4.165 4.165 1.778 1.778 1.713 1.713 1.713 1.713 1.284 1.16 1.16 1.16 1.16 1.16] ms

and for ICI

$T_{int}$ = 0.663161278 ms

$T_{int3dB}$ = [2.457 2.445 2.444 2.610 2.651 2.137 2.134 2.142 1.979 1.945 1.963 2.955 2.915] ms

# 5. Brightness temperature simulation

The BT and its uncertainty simulated from RS profiles are computed using the GRUAN processor (Carminati et al., 2019). GRUAN processor has been developed to collocate GRUAN radiosonde profiles and NWP model fields, to simulate top-of atmosphere BT at frequencies used by space-borne instruments, and to propagate GRUAN uncertainties in simulated BT. GRUAN processor has been modified for the purposes of VICIRS, starting a new branch, currently at version 6.3.b.0.1. This version uses the latest version of RTTOV (v13.2) and simulates BT from GRUAN/RHARM RS without using information from spatially and temporally collocated NWP profiles or using NWP profiles. When the GRUAN/RHARM RS profiles are processed in combination with NWP data, the NWP information is used for:

- filling the gap of RS surface parameters. Among these, the skin temperature ($T_{skin}$) can be determined in two ways :
  - $T_{skin} = T_{2m} + (T_{skin}(NWP) - T_{2m}(NWP))$ where $T_{2m}$ is determined from RS and $T_{skin}(NWP), T_{2m}(NWP)$ are $T_{2m}$ $and$ $T_{skin}$ of the model;
  - $T_{skin} = T_{skin}(NWP)$;
- filling the gap of data over the RS top level;
- providing the ozone profile.

When NWP option is not activated

- surface parameter are determined directly from RS, considering the values closest to z=2m or to z=10m for wind components, where z is the *altitude field* in GRUAN RS and *geopotential_height field* in RHARM RS;
- the RTTOV reference ozone profile is used.

In the GRUAN processor an internal loop has been introduced on the different satellite angles to take into account that the zenith and azimuth angles vary for each ICI/MWI channel.

Regarding the emissivity model used in RTTOV, SURFEM-Ocean (Kilic et al, 2022) is chosen for sea. SURFEM-Ocean is a new microwave sea surface emissivity model available in RTTOV v13.2 valid across 0.5-700 GHz frequencies that should replace all FASTEM and TESSEM2 versions (https://nwp-saf.eumetsat.int/site/download/documentation/rtm/docs_rttov13/users_guide_rttov13_v1.2.pdf, Hocking et al. 2022b). The emissivity model for land/ice is the TELSEM2 (Wang et al, 2016). *RTTOV v13 Users Guide* (2022) recommends TELSEM2 emissivity atlas instead of FASTEM land/sea-ice parameterization that will be deprecated in the future RTTOV versions.

# 6. Multi-source correlative methodology for RS, NWP and SAT

A multisource correlative methodology analysis (MCMA) has been developed to analyze the three collocated sources of information (i.e. RS, NWP and MWI and/or ICI). It allows for the characterization of the error structure of three collocated (in space and time) measuring systems. In the following sections the mathematical formalism underpinning MCMA is described with emphasis to the assumptions required to properly implement MCMA.

## 6.1 Assumptions

We assume to have three measuring systems $x_i$ with the index $i$=1, 2,3 (Stoffelen et al., 1998). Note that here, the term "measuring systems" is not restricted to actual measured data only but it can be extended to a numerical system that simulates a measured quantity, as well. For example, for our purposes, $x_i$ can refer to RS, NWP and a specific channel of MWI or ICI Satellite radiometer in terms of BT (K).
Each of the terms can be thought as the result of measuring process that introduces some amplification ($a_i$), biases ($b_i$) and noise ($\varepsilon_i$), to a true, but unknown, geophysical quantity ($t$):

$$x_i = b_i + a_i\, t + \varepsilon_i \tag{6.1}$$

where:

$a_i$ calibration scaling of measuring system $i-th$
$b_i$ calibration bias of measuring system $i-th$
$t$ unobserved truth which is common to all the measuring systems
$\varepsilon_i$ measurement random error of system $i-th$

Some assumptions on the different terms of (6.1) are required to greatly simplify the mathematics and arrive at quantifying the error variance ($\sigma_{\varepsilon i}^2$ ) which is one of the ultimate goals of MCMA. Some other additional assumptions are required to estimate the calibration parameters of two measuring systems out of three. The main MCMA assumptions are:
*Assumption1 (A1)*: eq. (6.1) holds, that implies linearity between $x_i$ and $t$ holds as well.
*Assumption2 (A2)*: the error $\varepsilon_i$ is zero average random error, that means <$\varepsilon_i$>=0 where <·> is the average operator.
*Assumption3 (A3)*: the error $\varepsilon_i$ is independent by the truth, $t$, which means <$\varepsilon_i\ t$>=0
*Assumption4 (A4)*: the errors of the various measuring systems are independent of each other, i.e.: <$\varepsilon_i\ \varepsilon_j$>=0 with $i \neq j$ and $(i, j)$ describing all the combinations in the interval from 1 to 3.

*Assumption5 (A5)*: both $x_i$ and $\varepsilon_i$ are stationary processes, i.e. they should have constant mean and standard deviation in the analyzed domain.
*Assumption6 (A6)*: the three measuring systems, $x_i$, $i = 1,2,3$ must observe the same quantity.

The additional assumptions required to find $a_i$ and $b_i$ will be discussed later on.
About assumption (A4) it is critical and some theoretical tools exist to characterize the correlation term $<\varepsilon_i\ \varepsilon_j>$ when it is caused by common spatial scales shared by the measuring system involved. On assumption (A5), for our purposes, a way to circumvent the stationarity issue could be to select the input measurements $x_i$ so that they comply with the stationarity requirement. Practically we could reorganize (for example randomly re-sampling) the input dataset of measurements $x_i$ with respect to their spatial and temporal acquisition index so that any non-stationarity is leveled or at least made less prominent.

## 6.2 Random error estimation

Under the assumptions A1-A6, and assuming that the error variances are referred to the observation scale of the third measuring systems, it can be demonstrated that the error variance of the three measuring systems in (6.1) can be estimated ($\hat{\cdot}$) as follows:

$$\hat{\sigma}^2_{\varepsilon_1} = \sigma^2_{x_1} - \frac{C_{13}}{C_{23}}(C_{12} - e_{12}) \tag{6.2a}$$

$$\hat{\sigma}^2_{\varepsilon_2} = \sigma^2_{x_2} - \frac{C_{23}}{C_{13}}(C_{12} - e_{12}) \tag{6.2b}$$

$$\hat{\sigma}^2_{\varepsilon_3} = \sigma^2_{x_3} - C_{13}\ C_{23}\left(\frac{1}{C_{12} - e_{12}}\right) \tag{6.2c}$$

In eq.(7.2), $\hat{\sigma}^2_{xi}$ is the estimated variances of the measured quantities from the $i-th$ measuring system whereas $C_{ij}$ are the covariances terms defined as usual:

$$C_{ij} = \langle (x_i - \langle x_i \rangle)\big(x_j - \langle x_j \rangle\big)\rangle \tag{6.3}$$

More elaborated arguments need to be spent on the term $e_{12}$. The latter is defined as the covariance of errors of systems 1 and 2:

$$e_{12} = \langle \varepsilon_1\ \varepsilon_2 \rangle = \rho_{12}\ \sigma_{\varepsilon_1}\ \sigma_{\varepsilon_2} \tag{6.4}$$

Where $\rho_{12}$ is the correlation coefficients between $\varepsilon_1$ and $\varepsilon_2$. Then $e_{12} \neq 0$ seems to violate the MCMA assumption 4. However, as will be clearer in a later section, the MCMA theory can accept some measurement errors to be correlated to describe some representativeness errors in the measurements. In eq. (6.2) it is implicitly assumed that the systems number 3 (eg. MWI of ICI) has the lower spatial resolution compared to the other two systems, and it is taken as reference for the scale of analysis (i.e. the error variances, $\hat{\sigma}^2_{\varepsilon i}$ , will be referred to the poorer spatial scale of the system 3 and consequently its representativeness error is zero). Consequently, measurements from systems 1 (i.e RS) and 2 (i.e. NWP), thanks to their higher variability, which is caused by their higher resolution than system 3, will pay for an additional error. Consequently, system 1 will pay for the largest representativeness error than system 2 and 3. Such extra errors depend on the way the system 1 and 2 observe (i.e. represent) the scene at the coarser reference scale of system 3, and for this reason it is referred as representativeness error in the MCMA framework. The representativeness error is then included in the term $e_{12}$ (6.2) since it contributes to increasing the error variance $\hat{\sigma}^2_{\varepsilon 1}$ and $\hat{\sigma}^2_{\varepsilon 2}$ (i.e $C_{12} - e_{12}$)is lowering as $e_{12}$ is increasing, thus making $\hat{\sigma}^2_{\varepsilon 1}$ closer to $\hat{\sigma}^2_{x1}$ and lowering $\hat{\sigma}^2_{\varepsilon 3}$ with similar reasoning for the system 2). Estimation of $e_{12}$ can be critical and requires spatial spectral analysis of the data for systems 2 and 3. Obviously, a different choice of the reference scale of analysis will lead to a different formulation of (6.2). Note for what just discussed above, the term $e_{12}$ is implicitly referring to the error correlation caused by the common spatial scales shared by the measuring systems involved. However, there could be an additional factor that tends increasing the term $e_{12}$. Indeed, RS and NWP (i.e. systems 1 and 2, respectively) share the same RTM to map the measured geophysical quantities into the BT domain, and consequently both BT from RS and NWP will be equally affected by the error introduced by RTE ($\varepsilon^{RTE}$). In other words, RTM introduces a unitary error correlation in eq. (6.4) reducing it to $e_{12}$=$\sigma^2_{\varepsilon RTE}$ with $\rho_{12} = 1$; $\sigma_{\varepsilon_1} = \sigma_{\varepsilon_2} = \sigma_{\varepsilon RTE}$. Values of $\sigma_{\varepsilon RTE}$ can be inferred from literature (e.g. Gallucci et al., 2023) and easily ingested in the TC procedures. Actually, estimates of $\sigma_{\varepsilon RTE}$ for MWI and ICI channels are described in the next Section 7 and shown in Figures 7.1 and 7.2 and listed in Tables 7.1 and 7.2 (note that in section 7, $\sigma_{\varepsilon RTE}$ is labeled as $\sigma_{BT}$).

## 6.3 Correlation coefficient estimation

A second output quantity provided by the MCMA is the correlation coefficient ($\rho_{t,i}$) between the actual unobserved value, $t$, and each input time series, $x_i$ (McColl et al., in 2014):

$$\hat{\rho}_{t,1} = \frac{1}{\hat{\sigma}_{x1}} \sqrt{\frac{(C_{12} - e_{12})\, C_{13}}{C_{23}}} \quad (6.5a)$$

$$\hat{\rho}_{t,2} = \frac{1}{\hat{\sigma}_{x2}} \sqrt{\frac{(C_{12} - e_{12})\, C_{23}}{C_{13}}} \quad (6.5b)$$

$$\hat{\rho}_{t,3} = \frac{1}{\hat{\sigma}_{x3}} \sqrt{\frac{C_{23}C_{13}}{(C_{12} - e_{12})}} \tag{6.5c}$$

These quantities are additional metrics to characterize the co-variability of the three measuring systems with the unobserved truth, providing important new information about their performance. Another quantity that can be derived by the correlation coefficients is the signal to noise ratios of the three systems defined as the ratio between the signal and the error averaged squared value:

$$SNR_i = \frac{\langle (x_i')^2 \rangle}{\langle (\varepsilon_i)^2 \rangle} = \frac{\rho_{t,i}^2}{1+\rho_{t,i}^2} \tag{6.6}$$

Where $x'_i$ is the signal part of $x_i$ (i.e. $x'_i = b_i + a_i\, t$ ).

## 6.4 Calibration parameter estimation

Another important achievement of MCMA is the possibility to calculate the calibration parameters $a_i$ and $b_i$. This is done by assuming one of the three systems is perfectly calibrated. Here we assume, without loss of generality, the system 1 being perfectly calibrated (i.e. $a_1 = 1$ and $b_1 = 0$). Under such assumption it can be demonstrated that estimated parameters are:

$$\hat{a}_2 = \frac{C_{23}}{C_{13}} \tag{6.7a}$$

$$\hat{a}_3 = \frac{C_{23}}{(C_{12} - e_{12})} \tag{6.7b}$$

and

$$\hat{b}_2 = \langle x_2 \rangle - \hat{a}_2 \langle x_1 \rangle \tag{6.8a}$$

$$\hat{b}_3 = \langle x_3 \rangle - \hat{a}_3 \langle x_1 \rangle \tag{6.8a}$$

Note that any known bias or scale parameter for the reference measuring system 1 must be compensated for before implementing eq.s (6.7) and (6.8).

# 7. Uncertainty analysis

Section 5 of [AD-7] introduces the metrological approach to the uncertainty analysis of the vicarious calibration using radiosonde observations. Section 5 also reviews the identified sources of uncertainty, which are summarized in Table 5.2 of [AD-7], together with the relevant references and the status of understanding. The survey indicated that some sources of uncertainty have been quantified in literature, but most of them have not. As stated by Calbet et al. (2017), it is unlikely that all the sources can be characterized fully, which somehow prevents a full metrological closure. For example, the correlation of radiosonde uncertainty between levels is not completely understood, and just that makes an enormous difference in the estimation of total uncertainty. Nevertheless, the knowledge gap analysis performed within VICIRS aimed to advance the awareness and knowledge of the contributing uncertainties, and to verify the consistency of independent measurements, making conclusions consistent to the extent possible.

Among the identified sources of uncertainty there are the absorption model and surface emissivity, which likely dominate the uncertainty budget for window channels. The absorption model uncertainty has been evaluated in a previous EUMETSAT study (Gallucci et al., 2024). Preliminary results were reported in Figure 5.4 of [AD-7], showing the uncertainty of atmospheric absorption models for simulations of upwelling brightness temperature (BT) at top of the atmosphere due to 135 dominant $H_2O$ and $O_2$ spectroscopic parameters. The adopted geometry mimics the observations from MWI and ICI, i.e., down-looking from top-of-the-atmosphere with 53° incident angle. The emissivity of a sea surface (covering 72% of the globe) is considered, assuming typical conditions (8 m/s wind speed; 290 K sea surface temperature; 35 PSU salinity). The uncertainty has been evaluated for six typical climatology conditions (tropical, midlatitude summer, midlatitude winter, sub-arctic summer, sub-arctic winter, U.S. standard). The corresponding uncertainty on simulated BT for MWI and ICI has been calculated by convoluting the spectra in Figure 5.4 of [AD-7] within the instrument bandpass filters. The channel convolution is performed by first-order approximation, i.e., a box-average of the original calculations at 50 MHz spectral resolution falling within the channel bandwidth. The number of frequencies falling within the bandwidths goes from 7 to 200. The uncertainty of simulated BT for MWI and ICI channels, considering their bandpass filters, is reported in the following Figures 7.1 and 7.2, as well as in Table 7.1 and 7.2.

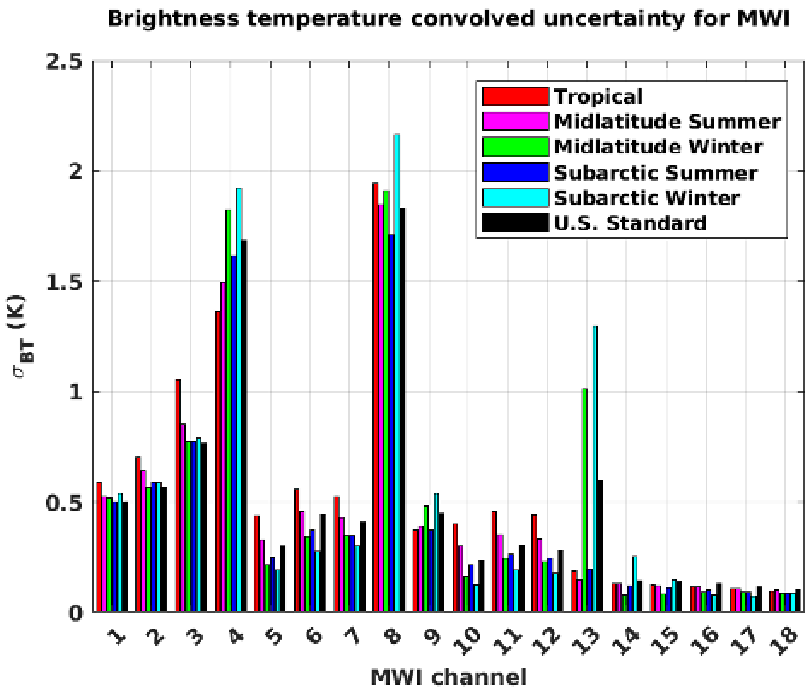


**Figure 7.1** Uncertainty of simulated BT for MWI channels due to uncertainties in $H_2O$ and $O_2$ parameters. Down-looking view from top-of-the-atmosphere with 53° incident angle. Sea surface emissivity at typical conditions (8 m/s wind speed; 290 K sea surface temperature; 35 PSU salinity). Color bars indicate six typical climatology conditions (tropical, midlatitude summer, midlatitude winter, sub-arctic summer, sub-arctic winter, U.S. standard).

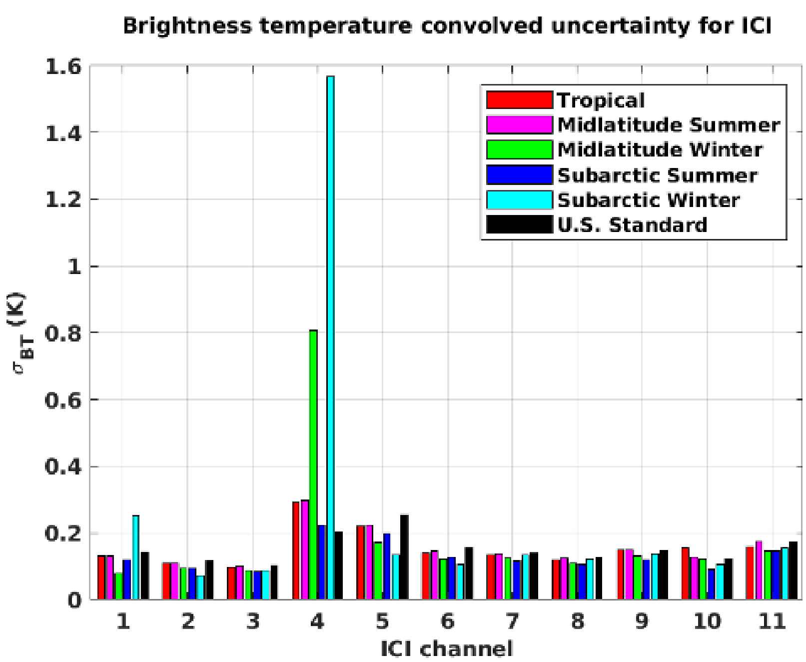


**Figure 7.2** As in Figure 7.1 but for ICI channels.

**Table 7.1** Uncertainty for simulated TOA downward-looking BT(K) at MWI channels (GHz) due to uncertainties in $H_2O$ and $O_2$ parameters. Six climatological atmospheric conditions are considered: tropical, midlatitude summer, midlatitude winter, sub-arctic summer, sub-arctic winter, U.S. standard.

| Channel (GHz) | Tropical | MidlatSum | MidlatWint | SubArcticS | SubArcticW | USstd |
|---|---|---|---|---|---|---|
| **18.7** | 0.59 | 0.52 | 0.52 | 0.50 | 0.54 | 0.50 |
| **23.8** | 0.70 | 0.64 | 0.57 | 0.59 | 0.59 | 0.57 |
| **31.4** | 1.05 | 0.85 | 0.78 | 0.77 | 0.79 | 0.77 |
| **50.3** | 1.37 | 1.50 | 1.82 | 1.61 | 1.92 | 1.69 |
| **52.8** | 0.44 | 0.33 | 0.22 | 0.25 | 0.19 | 0.30 |
| **53.24** | 0.56 | 0.46 | 0.34 | 0.37 | 0.28 | 0.44 |
| **53.75** | 0.52 | 0.43 | 0.35 | 0.35 | 0.30 | 0.41 |
| **89** | 1.94 | 1.85 | 1.91 | 1.71 | 2.16 | 1.83 |
| **118.75±3.2** | 0.37 | 0.39 | 0.48 | 0.37 | 0.54 | 0.45 |
| **118.75±2.1** | 0.40 | 0.30 | 0.16 | 0.22 | 0.13 | 0.23 |
| **118.75±1.4** | 0.46 | 0.35 | 0.24 | 0.26 | 0.19 | 0.30 |
| **118.75±1.2** | 0.45 | 0.34 | 0.23 | 0.24 | 0.18 | 0.28 |
| **165.5±0.725** | 0.19 | 0.15 | 1.01 | 0.20 | 1.3 | 0.6 |
| **183.31±7** | 0.13 | 0.13 | 0.08 | 0.12 | 0.25 | 0.14 |
| **183.31±6.1** | 0.12 | 0.12 | 0.08 | 0.11 | 0.15 | 0.14 |
| **183.31 ± 4.9** | 0.12 | 0.12 | 0.09 | 0.10 | 0.08 | 0.13 |
| **183.31 ± 3.4** | 0.11 | 0.11 | 0.09 | 0.09 | 0.07 | 0.11 |
| **183.31 ± 2** | 0.10 | 0.10 | 0.09 | 0.09 | 0.09 | 0.10 |

**Table 7.2** As in Table 7.1, but for ICI.

| Channel (GHz) | Tropical | MidlatSum | MidlatWint | SubArcticS | SubArcticW | USstd |
|---|---|---|---|---|---|---|
| **183.31±7.0** | 0.13 | 0.13 | 0.08 | 0.12 | 0.25 | 0.14 |
| **183.31±3.4** | 0.11 | 0.11 | 0.09 | 0.09 | 0.07 | 0.11 |
| **183.31±2.0** | 0.10 | 0.10 | 0.09 | 0.09 | 0.09 | 0.10 |
| **243±2.5** | 0.29 | 0.30 | 0.81 | 0.22 | 1.57 | 0.2 |
| **325.15±9.5** | 0.22 | 0.22 | 0.17 | 0.20 | 0.14 | 0.26 |
| **325.15±3.5** | 0.14 | 0.15 | 0.12 | 0.13 | 0.11 | 0.15 |
| **325.15±1.5** | 0.13 | 0.14 | 0.12 | 0.12 | 0.13 | 0.14 |
| **448±7.2** | 0.12 | 0.13 | 0.11 | 0.11 | 0.12 | 0.13 |
| **448±3.0** | 0.15 | 0.15 | 0.13 | 0.12 | 0.14 | 0.15 |
| **448±1.4** | 0.16 | 0.13 | 0.12 | 0.09 | 0.11 | 0.12 |
| **664±4.2** | 0.16 | 0.17 | 0.15 | 0.15 | 0.16 | 0.17 |

To our knowledge, the contribution of surface emissivity uncertainty to the uncertainty of brightness temperature simulations has not been quantified before. Quantification of the uncertainty affecting sea surface emissivity modeling is available at some channels and in certain conditions, while the uncertainty propagation to simulations is currently lacking. Therefore, a dedicated analysis has been performed within the VICIRS study. The surface emissivity in RTTOV can be modeled with different modules, e.g. FASTEM (Liu et al., 2011), TELSEM2 (Wang et al., 2017), TESSEM2 (Prigent et al., 2017), and SURFEM (Kilic et al., 2023). In terms of accuracy, TELSEM2 emissivity up to 325 GHz has been validated against airborne observations from the International Submillimeter Airborne Radiometer (ISMAR) and the Microwave Airborne Radiometer Scanning System (MARSS), reporting consistent estimates in spatially homogeneous regions, especially at 89 and 157 GHz (Wang et al., 2017). Fig.5.5 of [AD-7] shows histograms of retrieved minus TELSEM2 emissivity differences at 89, 118, 157, 183, 243, and 325 GHz channels (from Wang et al., 2017). Biases and standard deviation are of the order of 0.01 and 0.04, respectively. These values have been mapped into BT space to quantify the uncertainty due to the surface emissivity for the six typical climatology conditions introduced above (tropical, midlatitude summer, midlatitude winter, sub-arctic summer, sub-arctic winter, U.S. standard). Results are reported in Figure 7.3 and 7.4 for MWI and ICI, respectively, showing that the bias and standard deviations suggested by Wang et al., 2017 lead to large BT uncertainty, especially at lower frequency and most transparent channels. The same analysis, but for sea surface emissivity, considered the uncertainty derived from the analysis of Kilic et al. (2023), resulting in Figure 7.5 and 7.6 for MWI and ICI, respectively. Note that if conditions depart substantially from the six typical climatology introduced above, the effect of atmospheric opacity may be accounted for by multiplying the given uncertainty by a “surface efficiency” (0-1), e.g., a factor proportional to the normalized land surface contribution (LSC, see [AD-7]).

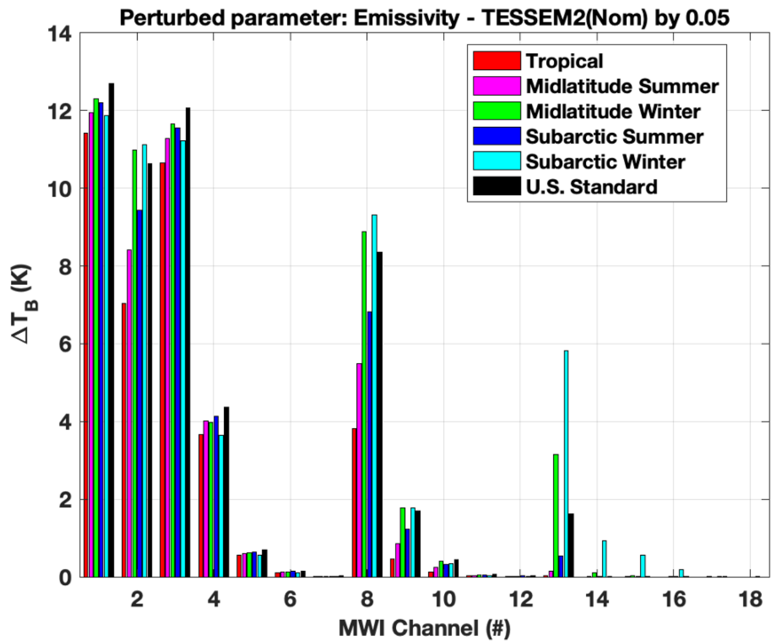


**Figure 7.3** Uncertainty of simulated BT for MWI channels due to uncertainties in land surface emissivity (Wang et al., 2017). Down-looking view from top-of-the-atmosphere with 53° incident angle. Sea surface emissivity at typical conditions (8 m/s wind speed; 290 K sea surface temperature; 35 PSU salinity) was used as baseline. Color bars indicate six typical climatology conditions (tropical, midlatitude summer, midlatitude winter, sub-arctic summer, sub-arctic winter, U.S. standard).

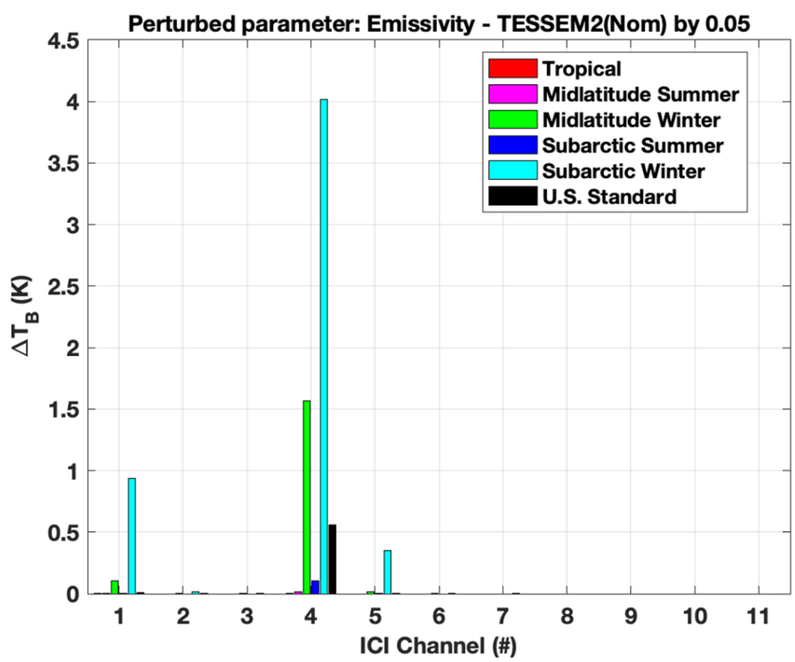


**Figure 7.4** As in Figure 7.3 but for ICI channels.

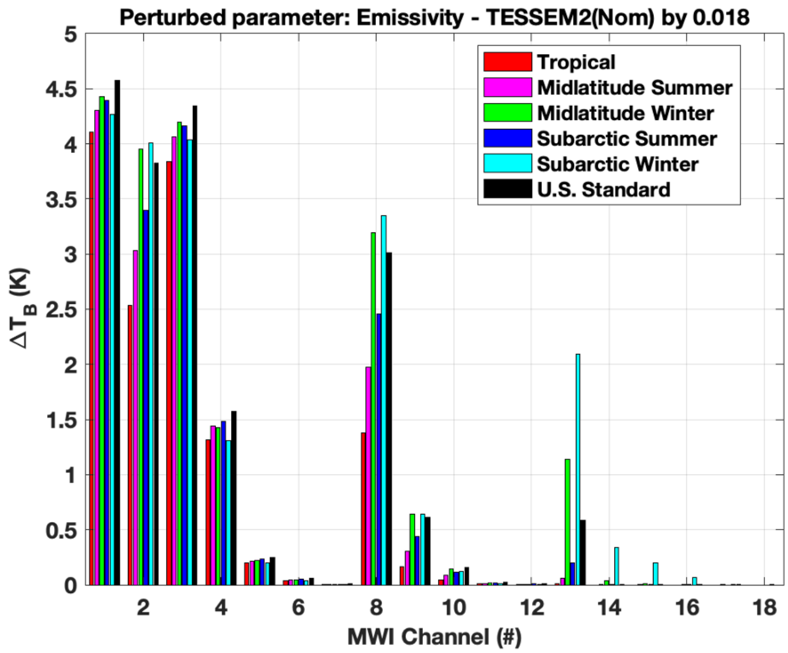


**Figure 7.5** As in Figure 7.3 but for sea surface emissivity (derived from Kilic et al., 2023).

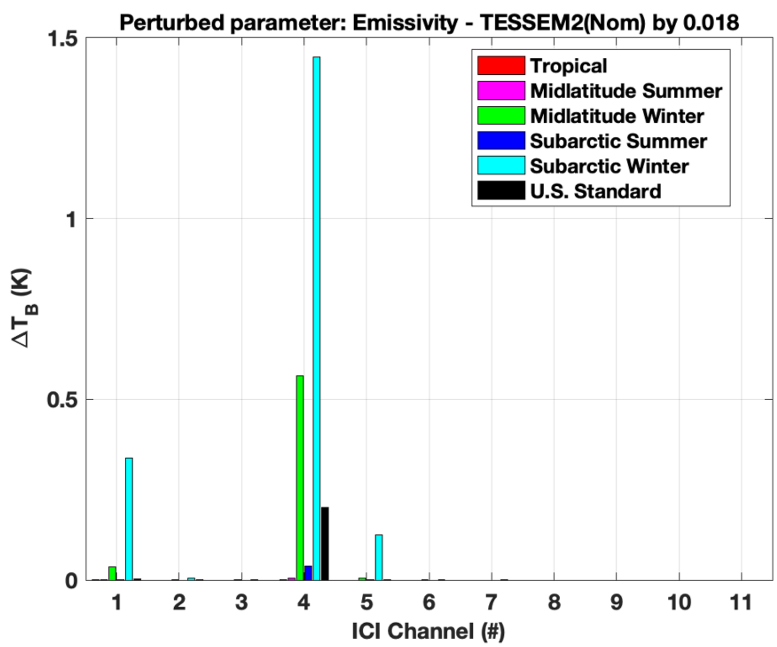


**Figure 7.6** As in Figure 7.4 but for sea surface emissivity (derived from Kilic et al., 2023).

The uncertainty analysis evaluated other sources of uncertainty, i.e.:

- colocation uncertainty: evaluated as the std of the BT within the TA;
- geolocation uncertainty: evaluated in analogy of the results by Papa et al. (2021), which reports an average geolocation uncertainty of 6 km, which has been mapped into the mean std of BT within a 3x5-IFOV box for each ICI & MWI channel;

- vertical interpolation uncertainty: evaluated extending to MWI and ICI channels the results reported in the NWP-SAF document for ATMS channels[1].

# 8. Match-up, bias and uncertainty analysis reporting in VICIRS tool

The match-up analysis consists in characterizing **each match-up for each frequency** by determining:

- the difference $TA\_RS\_SAT$ between the BT observed (BT_TA) and the BT simulated from radiosounding (BT_RS);
- the total uncertainty ($u\_all$) that includes all the independent sources of uncertainties described in Section 7

  $$u\_all = \sqrt{u\_col^2 + u\_obs^2 + u\_sim^2}$$

  where

  - $u\_obs = \sqrt{\left(NE\Delta T/\sqrt{nFOVs}\right)^2 + {u_{geol}}^2 + \cdots}$
  - $u\_col = \sqrt{SD\_TA(i,j)^2}$
  - $u\_sim = \sqrt{uBT\_RS^2 + uABS^2 + uEMIS^2 + uRTMlbl^2 + \ uRTMlev^2}$
- the coverage factor k, satisfying the following relation (Immler et al. 2010):

  $$TA\_RS < k \cdot u\_all.$$

The statistical analysis of the match-up dataset corresponding to the query criteria (related to the spatial and temporal coverage, the temporal difference between satellite overpass and sonde launch time, the TA type, the radiosonde archive, and the LF range), provides in output the following statistical quantities **for each frequency**:

- *BIAS_TA_RS***:** the mean value of TA_RS**;**

  $$BIAS\_TA\_RS = \frac{\sum_{i=1}^{nsample} TA\_RS}{nsample}$$

  where *nsample* is the number of the match-ups used for the statistics;

- *SD_TA_RS*: Standard Deviation of the *TA_RS*

  $$SD\_TA\_RS = \sqrt{\frac{\sum_{i=1}^{nsample}(BIAS(j) - TA\_RS(i,j))^2}{nsample - 1}}$$

- *u_BIAS*: uncertainty in the bias

[1] https://digital.nmla.metoffice.gov.uk/download/file/digitalFile_911bd873-f30f-4617-9810-ad73b5457ea1

$$u\_BIAS = SD\_TA\_RS/\sqrt{nsample}$$

- wBIAS**:** weighted BIAS of *TA_RS* (Moradi et al., 2010) accounting for the total uncertainty $u\_all$:

$$wBIAS = \frac{\sum_{i=1}^{nsample} w_i \cdot TA\_RS(i)}{\sum_{i=1}^{nsample} w_i},$$

  where

$$w_i = 1/(u\_all(i))^2$$

- SDw_TA_RS: Standard Deviation of TA_RS weighted on the total uncertainty *u_all*:

$$SDw\_TA\_RS = \sqrt{\frac{\sum_{i=1}^{nsample} w_{i,j} \cdot (wBIAS(j) - TA\_RS(i,j))^2}{\sum_{i=1}^{nsample} w_{i,j} - (\sum_{i=1}^{nsample} w_{i,j}^2 \,/\, \sum_{i=1}^{nsample} w_{i,j})}}$$

- *u_wBIAS***:** is the uncertainty of the weighted BIAS:

$$u\_wBIAS = \sqrt{\frac{1}{\sum_{i=1}^{nsample} w_{i,j}}}\,.$$

In detail,the following outputs are generated:

- SKEW_KURTOSIS_ **file_name**.png: shows Skew/Kurtosis for each frequency;

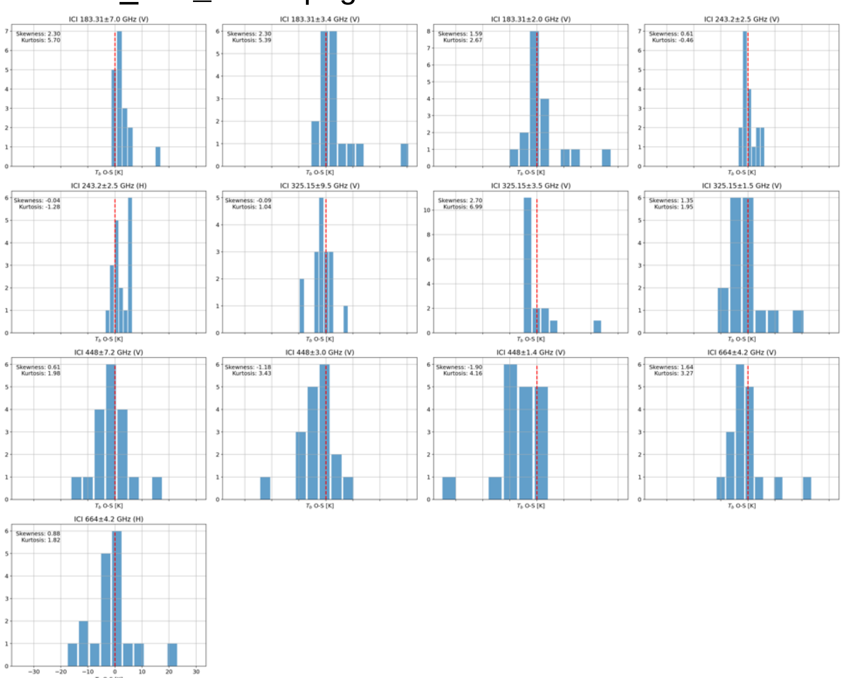


**Figure 8.1** Example of Skew/Kurtosis plotting for  ICI(L1B)-RHARM match-ups.

- SPATIAL_RS_PMIN_NLEV_ **file_name**.png: shows the spatial distribution of match-ups used for statistics and the histogram of RS Pmin and RS number of levels;

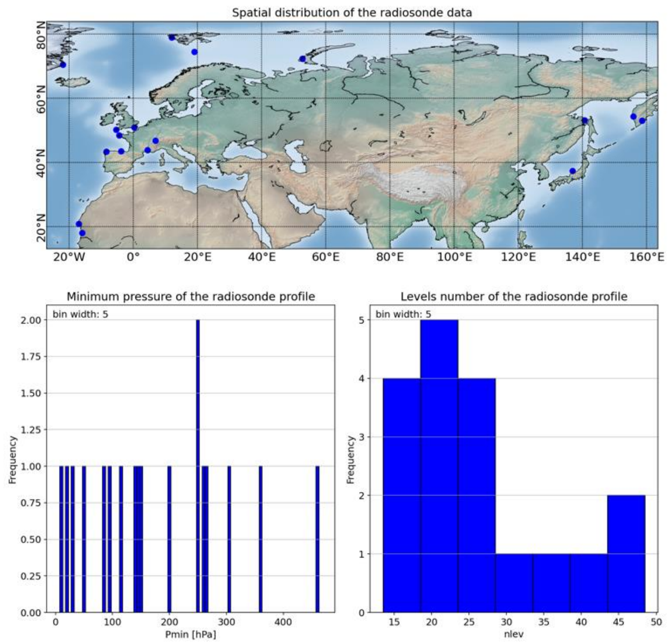


**Figure 8.2** Spatial distribution of ICI-RHARM match-ups (near coast) and histograms of Pmin and nlevs.

- UNC_**file_name**.png: shows the TA_RS_SAT and *u_all* indicating also K-FACTOR for each match-up and for each SAT frequency;

**Figure 8.3** Plots of BT(obs)-BT(sim) and related u_all for each ICI frequency (from ICI-RHARM statistics in [AD-10]). The color indicates the k factor, green when the measurements are consistent, orange when they are in agreement, red when they are no consistent and black plots are related to results that do not agree within k=3.

- BIAS_SD_**file_name**.png: *BIAS_TA_RS/SD_TA_RS/u_BIAS* plot for each frequency;

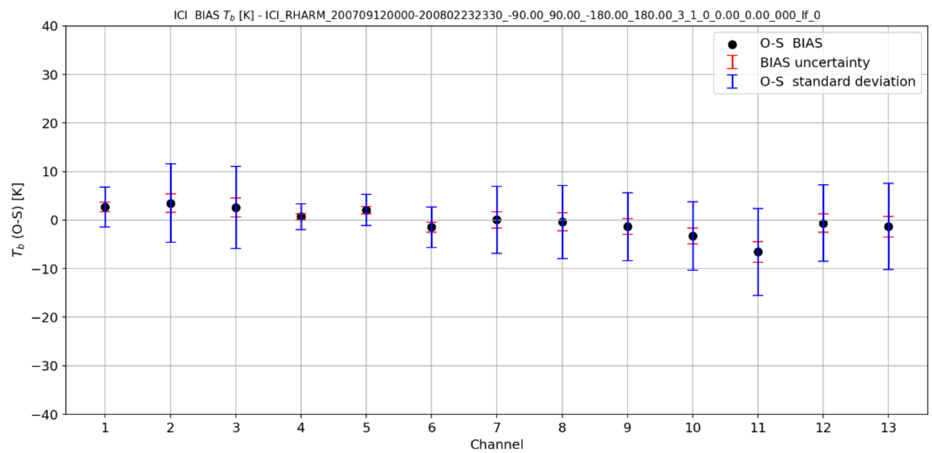


**Figure 8.4** Example of BIAS_TA_RS ± SD_TA_RS ±u_BIAS for ICI frequencies (from ICI-RHARM statistics in [AD-10])

- WBIAS_SD_**file_name**.png: *wBIAS/SDw_TA_RS/u_wBIAS* plot for each frequency;

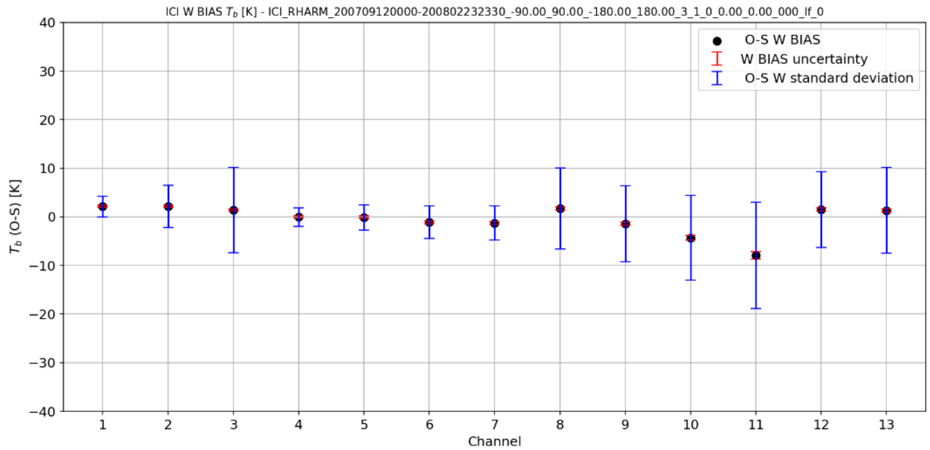


**Figure 8.5** Example of wBIAS ± SDw_TA_RS ±u_wBIAS for ICI frequencies (from ICI-RHARM statistics in [AD-10])

- scatter plot of BT observed versus BT simulated, colored differently to distinguish GRUAN sites (plot available only for GRUAN-SAT match-ups);

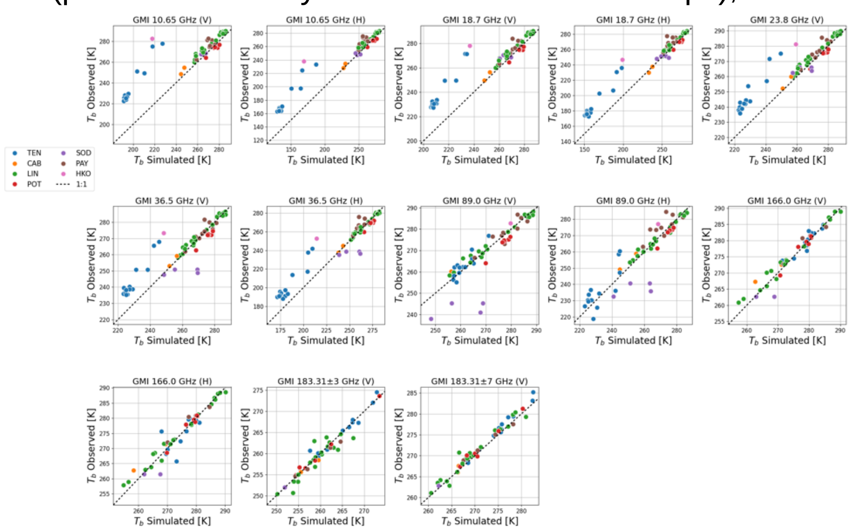


**Figure 8.6** Example of scatterplot of BT(Obs) vs BT(sim) (from GMI-GRUAN statistics in [AD-10]).

- RS statistics:
  - for all latitudes;
  - for polar latitudes;
  - for mid-latitudes;
  - for sub-tropical latitudes;
  - for tropical latitudes.

RHARM all sites

| | Polar latitude | Mid-latitude | Subtropical latitude | Tropical latitude | All latitude |
|---|---|---|---|---|---|
| **RS total (#)** | 27.0 | 43.0 | 9.0 | 13.0 | 92.0 |
| **RS discarded (#)** | 20.0 | 29.0 | 5.0 | 9.0 | 63.0 |
| **RS useful (#)** | 7.0 | 14.0 | 4.0 | 4.0 | 29.0 |
| **QC fails (%)** | 7.41 | 9.3 | 11.11 | 15.38 | 9.78 |
| **Cloudy fails (%)** | 66.67 | 60.47 | 44.44 | 53.85 | 59.78 |
| **AMD fails (%)** | 0.0 | 0.0 | 0.0 | 0.0 | 0.0 |
| **Total fails (%)** | 74.07 | 67.44 | 55.56 | 69.23 | 68.48 |

**Figure 8.7** Example of RS statistics for all RHARM RS used in ICI(MWI)/RHARM statistics [AD-10].

**file_name**=(H_)(MCM)*SAT_SondeArchive_startYYYYMMDDHHMM-endYYYYMMDDHHMM_LatSouthLatNorth LonEastLonWest_TemporaleDistance_TAtype_CloudyPercentage_LF_DL/NWPopt/Tskinopt* and **RS_statistic_filename**=*SondeArchive_startYYYYMMDDHHMM-endYYYYMMDDHHMM_ TemporaleDistance.nc*.

## References

Barlakas, V., A.J. Geer and P. Eriksson: Introducing hydrometeor orientation into all-sky microwave and submillimeter assimilation. Atmos. Meas. Tech., 14, 3427–3447, https://doi.org/10.5194/amt-14-3427-2021, 2021.

Bobryshev, O., S.A. Buehler, V.O. John, M. Brath, and H. Brogniez: Is There Really a Closure Gap Between 183.31-GHz Satellite Passive Microwave and In Situ Radiosonde Water Vapor Measurements?. IEEE Transactions on Geoscience and Remote Sensing,vol. 56, no. 5, pp. 2904-2910, doi: 10.1109/TGRS.2017.2786548, 2018.

Buehler, S. A., M. Kuvatov, V.O. John, U. Leiterer and H. Dier: Comparison of Microwave Satellite Humidity Data and Radiosonde Profiles: A Case Study. J. Geophys. Res., 109, D13103, https://doi.org/10.1029/2004JD004605, 2004.

Buehler, S. A., M. Kuvatov, T.R. Sreerekha, V.O. John, B. Rydberg, P. Eriksson, and J. Notholt: A cloud filtering method for microwave upper tropospheric humidity measurements, Atmos. Chem. Phys., 7, 5531–5542, https://doi.org/10.5194/acp-7-5531-2007, 2007.

Buehler, S. A., E. Defer, F. Evans, S. Eliasson, J. Mendrok, P. Eriksson, C. Lee, C. Jiménez, C. Prigent, S. Crewell, Y. Kasai, R. Bennartz, and A. J. Gasiewski: Observing ice clouds in the submillimeter spectral range: the CloudIce mission proposal for ESA's Earth Explorer 8, Atmos. Meas. Tech., 5, 1529–1549, https://doi.org/10.5194/amt-5-1529-2012, 2012.

Calbet, X., N. Peinado-Galan, P. Rípodas, T. Trent, R. Dirksen, and M. Sommer: Consistency between GRUAN sondes, LBLRTM and IASI. Atmos. Meas. Tech., 10, 2323–2335, https://doi.org/10.5194/amt-10-2323-2017, 2017.

Clain, G., H. Brogniez, V.H. Payne, V.O. John, and M. Luo: An Assessment of SAPHIR Calibration Using Quality Tropical Soundings, Journal of Atmospheric and Oceanic Technology, 32(1), 61-78. Retrieved Jan 18, 2023, from https://journals.ametsoc.org/view/journals/atot/32/1/jtech-d-14-00054_1.xml, 2015.

Carminati, F., S. Migliorini, B. Ingleby, W. Bell, H. Lawrence, S. Newman, J. Hocking,, and A. Smith: Using reference radiosondes to characterize NWP model uncertainty for improved satellite calibration and validation. Atmos. Meas. Tech., 12, 83–106, https://doi.org/10.5194/amt-12-83-2019, 2019.

Dinnat, E., and Coauthors, 2023: PARMIO: A Reference Quality Model for Ocean Surface Emissivity and Backscatter from the Microwave to the Infrared. Bull. Amer. Meteor. Soc., 104, E742–E748, https://doi.org/10.1175/BAMS-D-23-0023.1.

Evans, K. F., Wang, J. R., Racette, P. E., Heymsfield, G., and Li, L.: Ice Cloud Retrievals and Analysis with Data from the Conical Scanning Submillimeter Imaging Radiometer and the Cloud Radar System during CRYSTAL-FACE, J. Appl. Meteorol., 44, 839–859, 2005.

Gallucci D., D. Cimini, S. Fox, P. Rosenkranz, M. Tretyakov, V. Mattioli, and F. Romano: Uncertainty of upwelling brightness temperature simulations due to sensitivity to atmospheric gas spectroscopic parameters, in preparation, 2023.

Gong, J. and Wu, D. L.: Microphysical properties of frozen particles inferred from Global Precipitation Measurement (GPM) Microwave Imager (GMI) polarimetric measurements, Atmos. Chem. Phys., 17, 2741–2757, https://doi.org/10.5194/acp-17-2741-2017, 2017.

Hocking, J., R. Saunders, A. Geer, and J. Vidot: RTTOV v13 Users Guide. Tech. Rep. NWPSAF-MO-UD-046, EUMETSAT Satellite Application Facility on Numerical Weather Prediction (NWPSAF), 2022b.

Hong, G., Heygster, G., Miao, J., and Kunzi, K. (2005), Detection of tropical deep convective clouds from AMSU-B water vapor channels measurements, J. Geophys. Res., 110, D05205, doi:10.1029/2004JD004949.

He, Q., Li, J., Wang, Z., & Zhang, L. (2022). Comparative study of the 60 GHz and 118 GHz oxygen absorption bands for sounding sea surface barometric pressure. Remote Sensing, 14(9), 2260.

John V. O. and S. A. Buehler, "The impact of ozone lines on AMSU-B radiances," Geophys. Res. Lett., vol. 31, p. L21 108, Nov. 2004.

Kilic L., C. Prigent1,2, C. Jimenez, E. Turner, J. Hocking, S. English, T. Meissner, E. Dinnat, Development of the SURface Fast Emissivity Model for Ocean (SURFEM-Ocean) based on the PARMIO2 radiative transfer mode, submitted to JGR Oceans, 2023.

Liu Q, Weng F, English SJ. 2011. An improved fast microwave water emissivity model. IEEE Trans. Geosci. Remote Sens. 49: 1238–1250, doi: 10.1109/TGRS.2010.2064779.

McColl, K.A., J. Vogelzang, A.G. Konings, D. Entekhabi, M. Piles, A. Stoffelen: Extended triple collocation: Estimating Errors and Correlation Coefficients with respect to an Unknown Target. Geophys. Res. Lett. 41, 6229–6236, 2014.

Moradi, I., S.A. Buehler, V.O. John, and S. Eliasson: Comparing upper tropospheric humidity data from microwave satellite instruments and tropical radiosondes, J. Geophys. Res., 115, D24310, doi:10.1029/2010JD013962, 2010.

Moradi, I., B. Soden, R. Ferraro, P. Arkin and H. Vömel: Assessing the quality of humidity measurements from global operational radiosonde sensors, J. Geophys. Res.-Atmos., 118, 8040– 8053, https://doi.org/10.1002/jgrd.50589, 2013a.

Moradi, I, S. A. Buehler, V. O. John, A. Reale and R. R. Ferraro: Evaluating Instrumental Inhomogeneities in Global Radiosonde Upper Tropospheric Humidity Data Using Microwave Satellite Data, IEEE Trans. Geosci. Rem. Sens., vol. 51, no. 6, pp. 3615-3624, June 2013, doi: 10.1109/TGRS.2012.2220551, 2013b.

Moradi, I., R. Ferraro, P. Eriksson, and F. Weng.: Intercalibration and Validation of Observations From ATMS and SAPHIR Microwave Sounders, IEEE T. Geosci. Rem. Sens., 53, 5915–5925, https://doi.org/10.1109/TGRS.2015.2427165, 2015.

Papa M.. V. Mattioli. J. Avbelj and F. S. Marzano. "Assessing the Spaceborne 183.31-GHz Radiometric Channel Geolocation Using High-Altitude Lakes. Ice Shelves. and SAR Imagery." IEEE TGRS. 2021. doi: 10.1109/TGRS.2020.3024677

Prigent, C., F. Aires, D. Wang, S. Fox, and C. Harlow: Sea-surface emissivity parametrization from microwaves to millimetre waves. Q.J.R. Meteorol. Soc., 143: 596-605. https://doi.org/10.1002/qj.2953, 2017.

Stoffelen, A.: Toward the true near-surface wind speed: Error modeling and calibration using triple collocation, J. Geophys. Res., 103, 7755–7766, doi:10.1029/97JC03180, 1998.

Wang, D., C. Prigent, L. Kilic, S. Fox, C. Harlow, C. Jimenez, F. Aires, C. Grassotti, and F. Karbou: Surface Emissivity at Microwaves to Millimeter Waves over Polar Regions: Parameterization and Evaluation with Aircraft Experiments, Journal of Atmospheric and Oceanic Technology, 34(5), 1039-1059, 2017.

Wu, Z., J. Li, Z. Qin: Development and Evaluation of a New Method for AMSU-A Cloud Detection over Land. Remote Sens. 13, 3646. https://doi.org/10.3390/rs13183646, 2021.

Yaping, Z., L. Jianwen, C. Zhoujie: Detection of Deep Convective Clouds Using AMSU-B and GOES-9 Data, China-Japan Joint Microwave Conference, pp. 278-281, doi: 10.1109/CJMW.2008.4772425, 2008.

Zhang, J., Chen, H., Li, Z., Fan, X., Peng, L., Yu, Y., and Cribb, M. (2010), Analysis of cloud layer structure in Shouxian, China using RS92 radiosonde aided by 95 GHz cloud radar, J. Geophys. Res., 115, D00K30, doi:10.1029/2010JD014030.

**[END OF D15: Algorithm Theoretical Basis Document]**